

Selecting an optimal aperture in Kirchhoff migration using dip-angle images^a

^aPublished in *Geophysics*, 78, no. 6, S243-S254, (2013)

Alexander Klovov and Sergey Fomel

ABSTRACT

We present a method for selecting a migration aperture in Kirchhoff migration. We first split migrated data into constant-dip-angle partial images. Then, in every partial image, we estimate the consistency between each event and the constant dip of the analyzed section. We filter out events whose slope is far from the corresponding dip. Stacking of the filtered partial images corresponds to migration having an optimal aperture. Synthetic and real data examples demonstrate that the proposed approach to migration-aperture optimization is able to reduce migration noise while preserving diffraction energy, which characterizes small geological objects and brings additional resolution to the image.

INTRODUCTION

Kirchhoff migration remains a popular tool for seismic imaging (Leveille et al., 2011). It handles every input trace separately, enabling the user to work with data sets of any configuration (including irregular geometry) and to apply target-oriented analysis. One of the features of Kirchhoff migration is its global aperture. The migration operator distributes energy throughout a wide area described by an impulse-response surface. However, a seismic image is constructed only by a local part of the surface that touches a reflector. The remainder does not make a constructive contribution and, even worse, may generate image artifacts (Sun, 1998; Hertweck et al., 2003).

The artifact problem can be solved by limiting migration aperture. Schleicher et al. (1997) analyzed influence of aperture parameters on imaging results and proposed a technique based on projected Fresnel zones for shortening the migration curve. After preliminary picking of target reflections and computing diffraction curves, they estimated the migration-aperture size by analytical equations. Sun (1998) analyzed the structure of a seismic image and proposed rules for its optimal construction. Two main principles were identified: (1) the tangent point between a diffraction curve and a reflector must be located in the central part of the aperture and (2) the aperture must be at least as large as the first Fresnel zone. Several methods were proposed to achieve these two objectives. Tillmanns and Gebrande (1999) detected instantaneous slowness in the data domain. Sun and Schuster (2001) described wave-path migration

smearing energy within a small zone centered on the specular reflection point and defined under a stationary-phase approximation. Lüth et al. (2005) smeared migrated multicomponent data only inside a Fresnel volume built around rays computed using polarization of the wavefield. Buske et al. (2009) constructed a Fresnel volume for single-component seismic data, determining the emergent angle by local slowness analysis. Tabti et al. (2004) worked with diffraction-operator panels and picked Fresnel apertures after preliminary low-pass filtering. Kabbej et al. (2007) introduced an attribute that characterizes the distance between a common-midpoint position and a currently imaged depth point then migrated the attribute and used it for weighting-function construction. Spinner and Mann (2007) used the common-reflection-surface operator to determine parameters for the optimal migration aperture. Alerini and Ursin (2009) estimated horizon slopes in the image domain.

The migrated dip-angle domain has properties that are favorable for taking both issues — the aperture position and its width — into consideration. In this domain, a reflection event has a concave shape with an apex whose position corresponds to the reflector dip (Audebert et al., 2002; Landa et al., 2008; Klokov and Fomel, 2012). The event summation in the dip-angle direction produces an image in accordance with the stationary-point principle (Bleistein et al., 2001). To limit aperture in the dip-angle domain and to restrict summation to stationary points, Bienati et al. (2009) applied an automatic slope estimation followed by muting. Aperture size was defined on the basis of wavelet bandwidth. Dafni and Reshef (2012) proposed analyzing migrated gathers simultaneously in dip-angle and scattering-angle directions.

A seismic wavefield may contain reflections and diffractions. There are a number of important differences between these two components (Klem-Musatov, 1994). One of the differences is that reflections require a narrow migration aperture, whereas diffractions require an aperture as wide as possible (while allowing matching of a diffraction curve). Therefore, all methods that imply migration-aperture limiting are oriented toward optimal imaging of reflection boundaries and not diffraction objects. Diffractions characterize small but important geological objects and play a significant role in imaging of rough reflection boundaries (Khaidukov et al., 2004). Their attenuation may cause a significant loss of resolution (Neidell, 1997). For image resolution to be preserved, a migration-optimization method should aim to protect the diffraction component. In this paper, we demonstrate an approach that allows us to achieve an optimal aperture size for reflection boundaries while also protecting the diffraction component. The main idea is analyzing slope information in constant-dip partial images.

DIFFRACTIONS AND REFLECTIONS IN CONSTANT-DIP PARTIAL IMAGES

Common-reflection-angle migration (Xu et al., 2001) can produce a set of dip-angle gathers in which traces are partial images of a fixed lateral position for different migration dips. At the same time, the migrated volume can be considered as a set

of constant-dip partial images. Integration of the partial images along the dip angle provides a seismic image:

$$I(\bar{\mathbf{x}}, z) = \int \hat{I}(\bar{\mathbf{x}}, z, \alpha) d\alpha, \quad (1)$$

where $\hat{I}(\bar{\mathbf{x}}, z, \alpha)$ is a true-amplitude partial image for migration dip α (Bleistein and Gray, 2002).

A dip-angle gather exposes the difference between reflections and diffractions (Audebert et al., 2002; Landa et al., 2008; Klokov and Fomel, 2012). Reflection events have a concave shape, and an image of a reflection boundary is constructed by a limited range of dip angles near the event apex. The effective range contains migrated impulses whose shift from the event apex does not exceed half the prevailing period. This area is equivalent to the Fresnel zone in the dip-angle domain. Diffraction events appear flat, however, which means that the full range of migration-dip angles provides an effective contribution to the image (Figure 1). Thus, an optimal migration aperture should simultaneously be limited for reflections and expanded for diffractions.

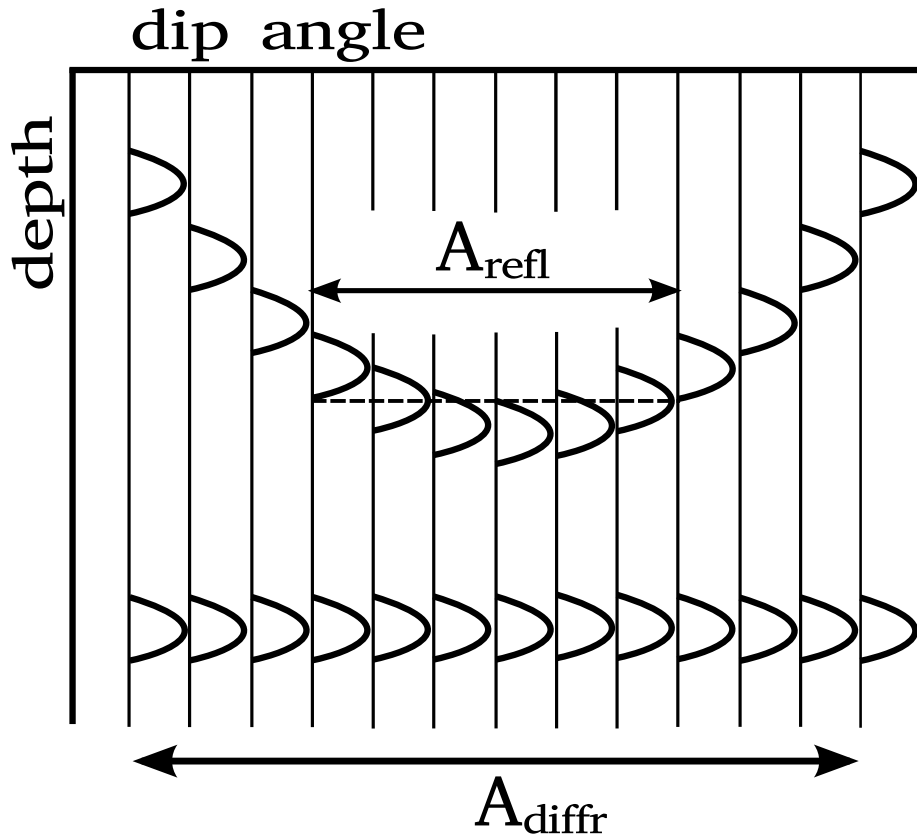


Figure 1: Reflection event and diffraction event in the 2D dip-angle gather.

In the constant-dip partial-image domain, reflections and diffractions appear different as well, although they have some analogous features. To examine this, let us

start with the simple case of zero-offset migration having the correct constant velocity. Similar derivations can be considered for prestack data.

A diffraction event behaves hyperbolically (Figure 2a). Its shape is defined by the following equation (see derivation in Appendix):

$$z(x_m) = (x_m - x_0) \tan \alpha + \sqrt{(x_m - x_0)^2 / \cos^2 \alpha + z_0^2}, \quad (2)$$

where α is the constant-dip of the partial image, x_m is an imaging position, and x_0 and z_0 are position and real depth of the diffraction point, respectively.

At the position of the diffraction point, when $x_m = x_0$, the event has the correct depth $z(x_m) = z_0$. The slope of the event at this point corresponds to the derivative:

$$\left. \frac{\partial z}{\partial x_m} \right|_{x_m=x_0} = \tan \alpha. \quad (3)$$

Equation 3 indicates that an effective part of a diffraction event, which corresponds to the correct position and contributes to the image, has the same slope as the migration dip, or the constant-dip of the corresponding partial image.

The response of a plane reflector in the constant-dip partial image is a segment. Let us consider a small part of the reflection boundary, which has a dip α_0 and lateral length d (Figure 2b). In the correct-constant-velocity case, coordinates of the segment edges after constant-dip migration can be defined by rotation around escape points y_1 and y_2 :

$$\bar{x}_1 = z_1 \frac{\sin \alpha_0 - \sin \alpha}{\cos \alpha_0}, \quad (4)$$

$$\bar{z}_1 = z_1 \frac{\cos \alpha}{\cos \alpha_0}, \quad (5)$$

and

$$\bar{x}_2 = z_2 \frac{\sin \alpha_0 - \sin \alpha}{\cos \alpha_0} + d, \quad (6)$$

$$\bar{z}_2 = z_2 \frac{\cos \alpha}{\cos \alpha_0}. \quad (7)$$

The migrated edge points define a segment, whose slope is

$$\tan \beta = \frac{\bar{z}_2 - \bar{z}_1}{\bar{x}_2 - \bar{x}_1} = \frac{\cos \alpha \sin \alpha_0}{1 - \sin \alpha \sin \alpha_0}. \quad (8)$$

Equation 8 illustrates some features of the migrated reflection boundary. For instance, a migrated horizontal reflector ($\alpha_0 = 0$) keeps the zero-slope independent of the migration dip.

Equation 8 also allows us to find the condition in which the migrated slope is consistent with the constant-dip partial image ($\beta = \alpha$). In this case,

$$\frac{\cos \alpha \sin \alpha_0}{1 - \sin \alpha \sin \alpha_0} = \frac{\sin \alpha}{\cos \alpha}. \quad (9)$$

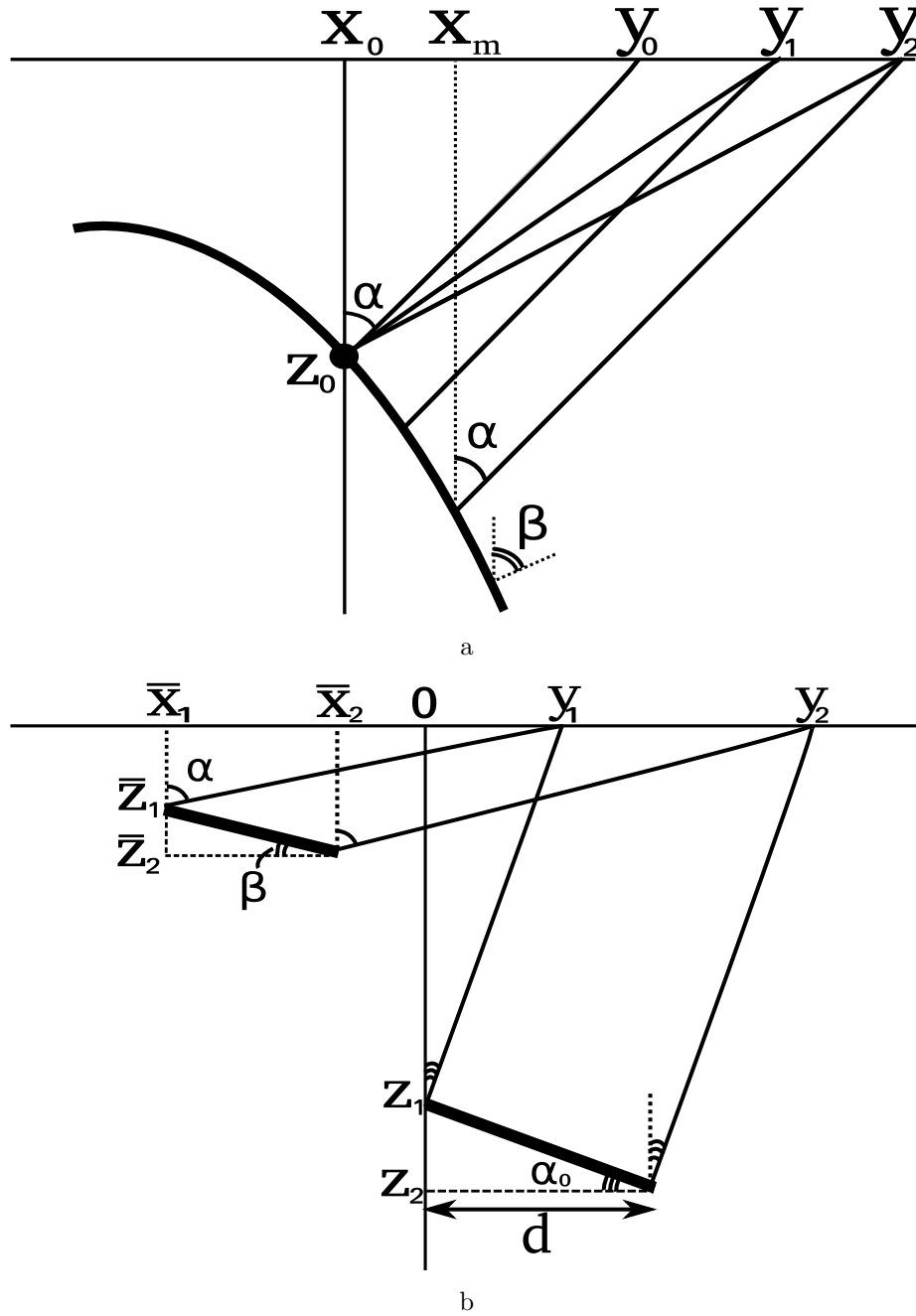


Figure 2: Constant-dip migration (scheme) of (a) a diffraction point and (b) a reflection boundary.

If α is derived from equation 9, note that the equation has only an $\alpha = \alpha_0$ solution. In other words, the slope of a migrated reflection event equals that of the migration dip only after migration with the correct dip. Such is the case when the segment corresponds to the stationary point and contributes to the image. Thus, an effective reflection event is consistent with the constant-dip partial image, as it is for diffractions. The derivation in the Appendix shows that this fact is true for curved reflectors as well.

To verify the assertions presented, we ran the following experiment. We put two reflectors and one scattering point in the constant-velocity field (Figure 3). One reflector is flat, and the second has a dip of 15 degrees. We assume that reflectivity is generated by density variations. The modeled zero-offset section is presented in Figure 4. We migrated the data using Kirchhoff common-angle migration with the correct velocity. Figure 5 displays the image and a dip-angle gather extracted from the position where the scattering point is located. The diffraction event appears flat in the dip-angle gather, as expected, while the reflection events have concave shapes. Figure 6 shows two partial images corresponding to 0 and 15 degrees. Note that reflection boundaries and an effective part of the diffraction event are consistent with the partial image — 0 and 15 degrees, respectively (the slope is indicated by dashed lines).

To represent a realistic situation, we placed the same reflectors and scattering point within a smoothed velocity field from the Marmousi model. Both reflection and diffraction events have complicated shapes in the data domain (Figure 7). Figure 8 displays the image and the dip-angle gather after migration with the correct velocity. The traveltimes for Kirchhoff angle-domain migration were computed by Huygens wavefront-tracing (Sava and Fomel, 2001), which allowed us to handle multiple arrivals. The diffraction event is flat, as it was in the constant-velocity example, but the shape of the reflection events appears much more complicated. The gather is contaminated by strong migration artifacts that produce noise in the image. Figure 9 shows two partial images corresponding to 0 and 15 degrees. Both images appear to be quite noisy. However, note that, even after migration with a complicated-velocity model, effective reflection events are consistent with the dips of partial images. The diffraction event at the scattering-point position has the appropriate slope as well (the slopes are indicated by dashed lines).

An event-slope-consistency analysis may provide information about separation between constructive and nonconstructive parts of migrated data. The key observation is that constructive reflection and diffraction events have slopes that are close to the constant-dip of the partial image. Slopes of nonconstructive events differ significantly from those of partial-image dips. Integration of constructive events only corresponds to migration having an optimal aperture.

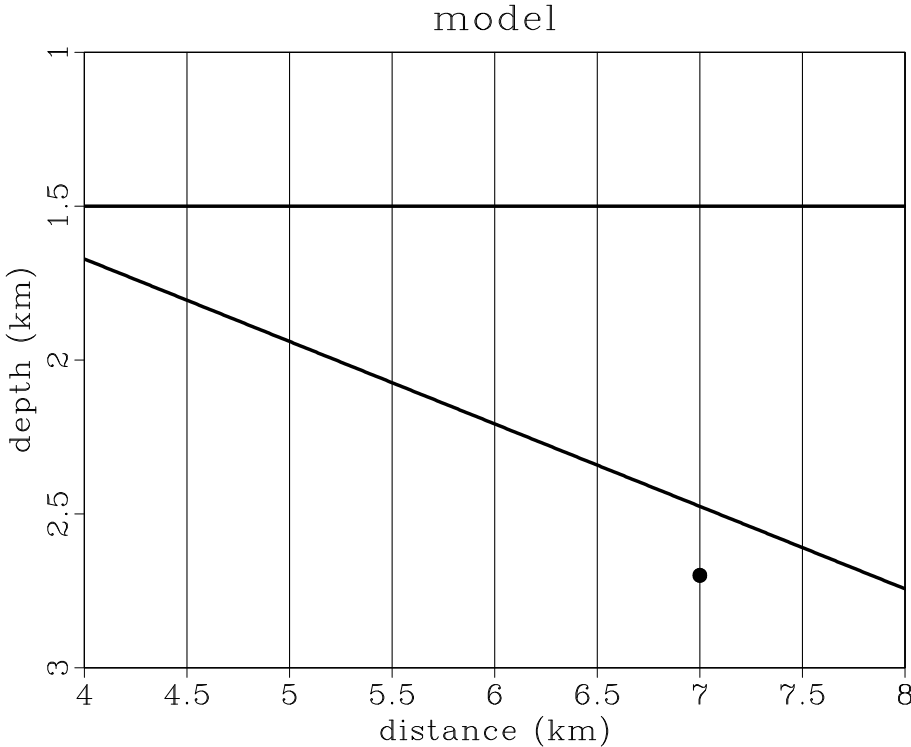


Figure 3: Theoretical model with two plane reflectors and one diffractor.

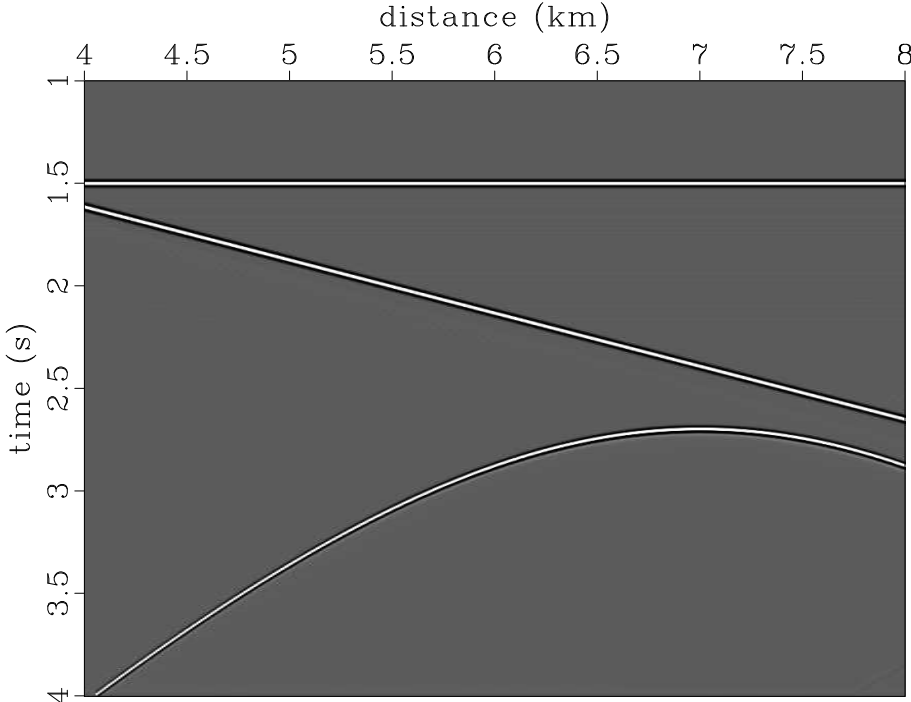


Figure 4: Zero-offset section corresponding to the constant-velocity model.

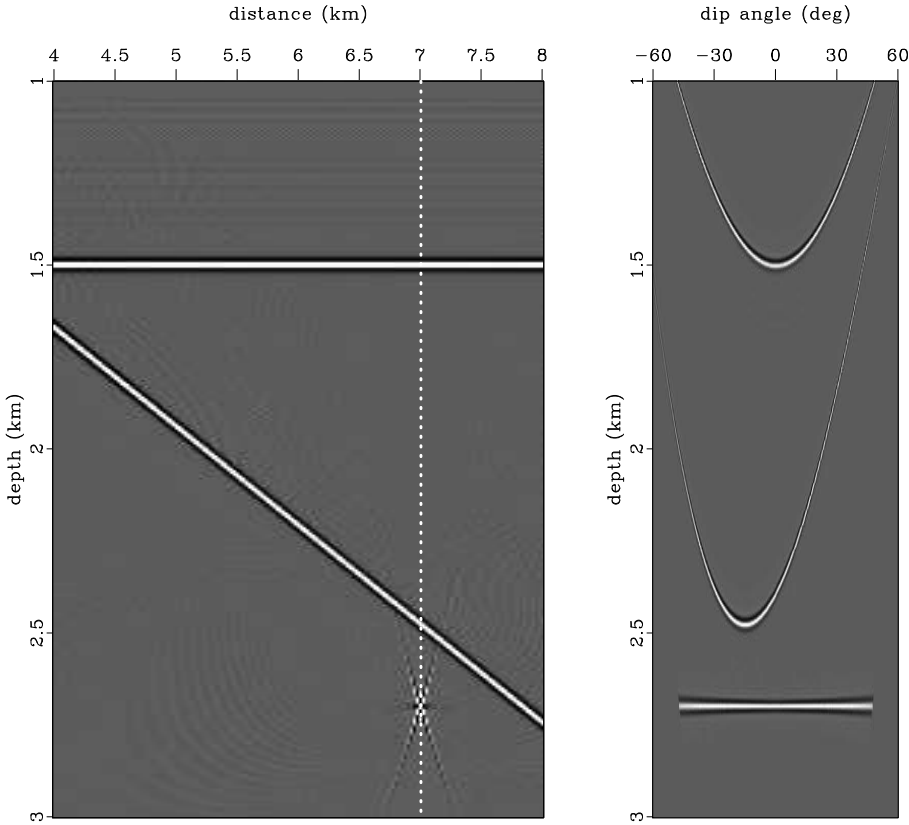


Figure 5: Depth-migrated image and common-image-gather in dip-angle domain corresponding to distance of 7 km.

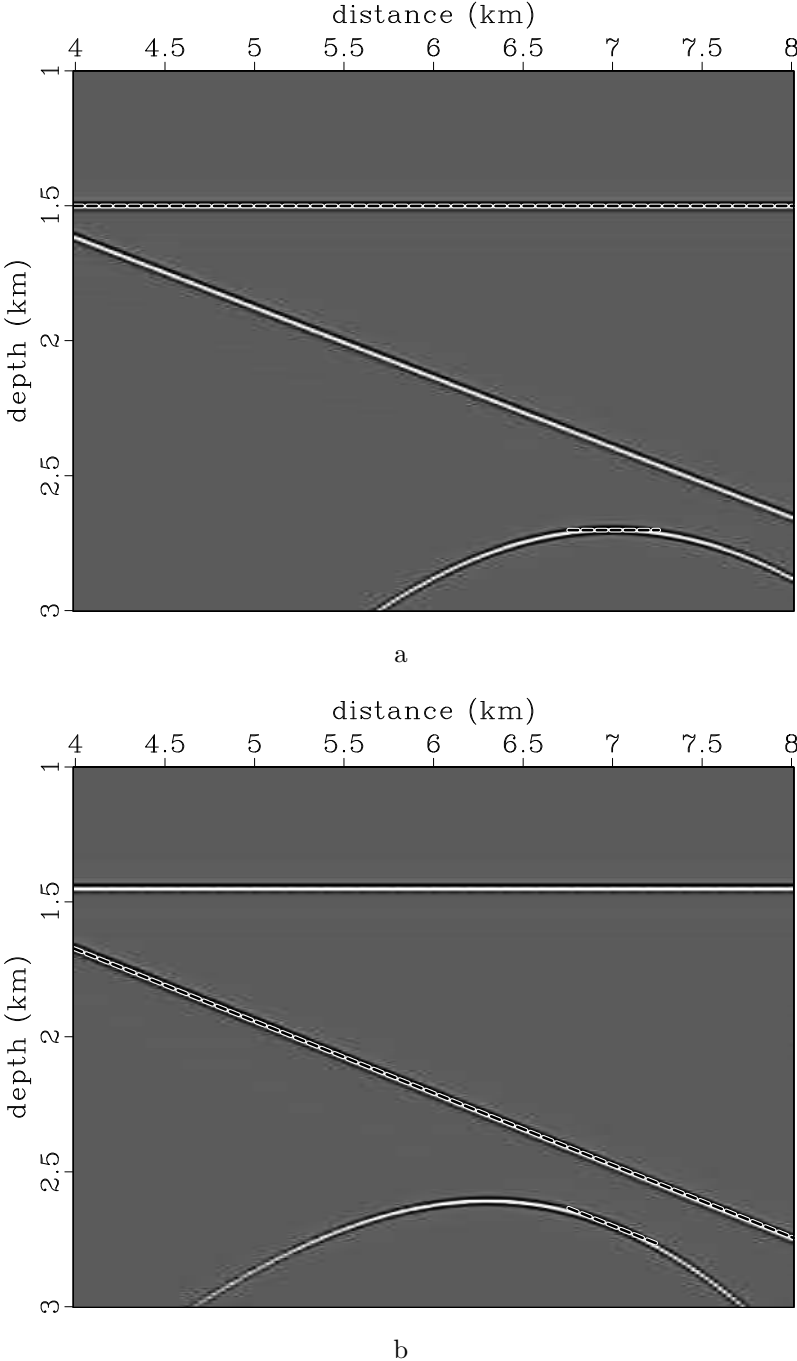


Figure 6: (a) Zero-degree partial image and (b) fifteen-degree partial image for the constant-velocity model.

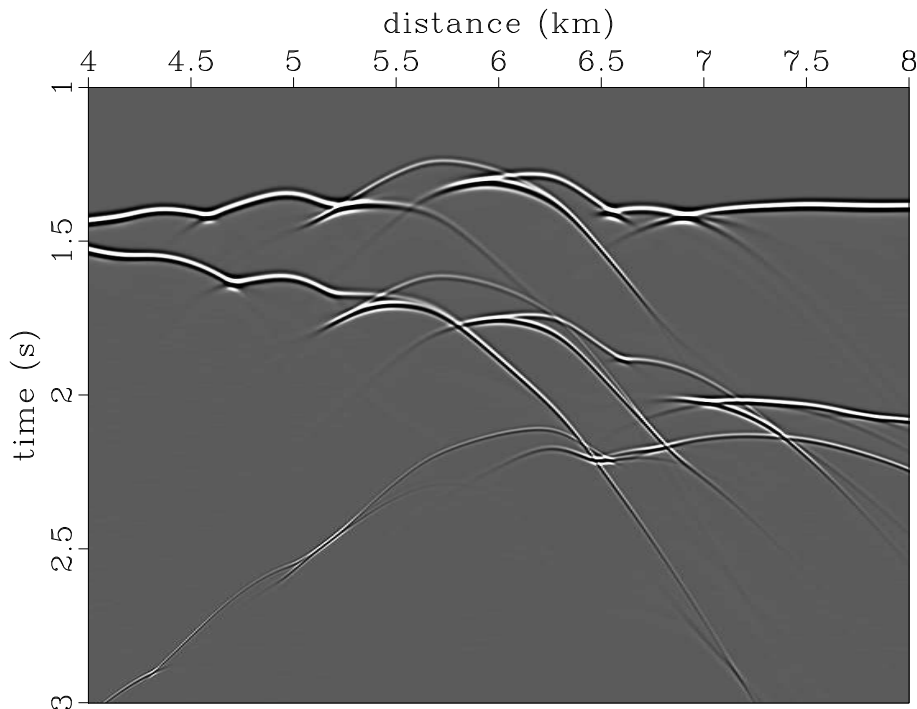


Figure 7: Zero-offset section corresponding to the Marmousi-velocity model.

SLOPE-CONSISTENCY ANALYSIS

One approach to analyzing constant-dip partial-image consistency is to measure the local slope in every partial image and to construct a taper function that is based on this measurement. The taper should protect events whose slope is close to the corresponding constant dip. Slopes that differ significantly from that of the constant dip should be attenuated. However, if conflicting dips occur in the partial image, dips estimation becomes a non-trivial task.

To avoid this issue, we estimate segment conformity with a partial image by stacking along a local trajectory defined by partial-image constant dip. Constructive segments match the trajectory that yields high values of coherency. On the other hand, destructive segments get stacked in the wrong direction and provide low values of coherence. Classic semblance (Taner and Koehler, 1969), as a coherence measure, can be used for defining a weight function. Weighting of migrated data corresponds to migration aperture optimization.

For illustration, we use the constant-dip partial images shown in Figure 9. They correspond to migration dips of 0 and 15 degrees, and we first apply local stacking along directions corresponding to 0 and 15 degrees, respectively. We extend stacking to the dip-angle direction as well. Effective contributions are locally plane in this direction, and local stacking along migration dips allows for signal enhancement. We measure coherency of the stacked data and get the semblance function $S(\alpha, z, x)$

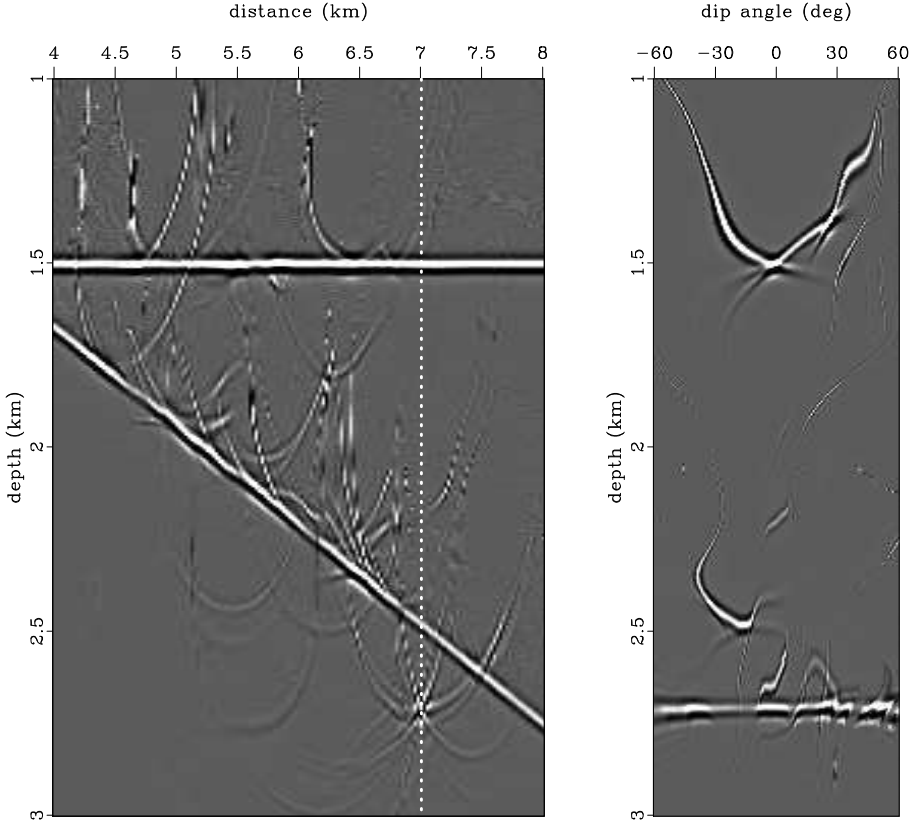


Figure 8: Depth-migrated image and common-image-gather in dip-angle domain corresponding to distance of 7 km.

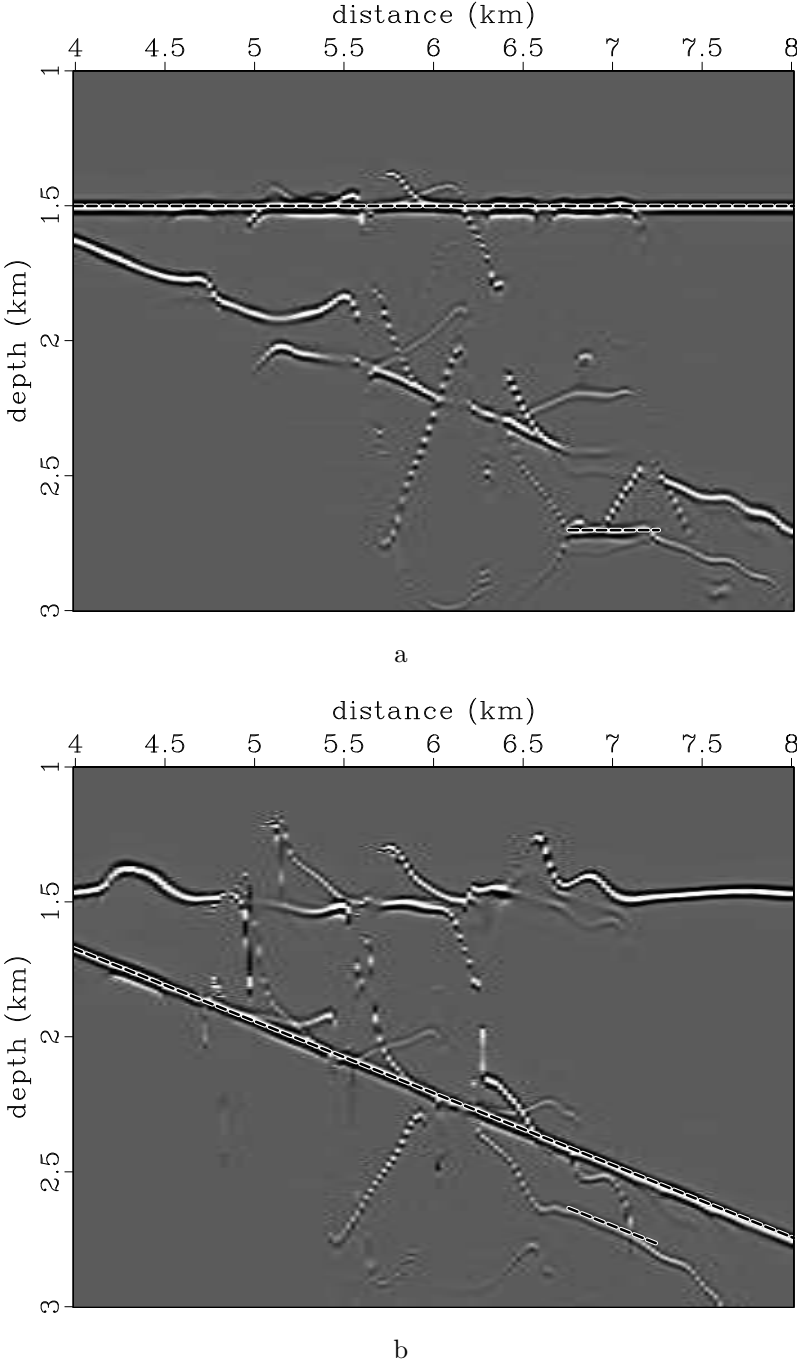


Figure 9: (a) Zero-degree partial image and (b) fifteen-degree partial image for the Marmousi-velocity model.

presented in Figure 10. High semblance values correspond to events consistent with the dips of partial images. The next step is to transform the semblance function to a weight function $W(\alpha, z, x)$, which should optimally handle migrated amplitudes. The weight should not change a plane diffraction event or an effective apex area of reflections. At the same time, the weight should smoothly attenuate away from the apexes so that edge effects can be eliminated (Hertweck et al., 2003). We define our weight function using the following thresholding rule:

$$W(\alpha, z, x) = \begin{cases} 1 & \text{for } S(\alpha, z, x) > s_2, \\ \frac{S(\alpha, z, x) - s_1}{s_2 - s_1} & \text{for } s_1 < S(\alpha, z, x) < s_2, \\ 0 & \text{for } S(\alpha, z, x) < s_1, \end{cases} \quad (10)$$

where s_1 and s_2 define two thresholds. Thus, weight function is defined by summation bases and thresholding parameters. In complex inhomogeneous media, these parameters depend on migrated data and can be estimated by trial and error. Local summation in the dip-angle direction can be performed along constructive parts of the reflection concave event, whose size is defined after analysis of migrated dip-angle gathers. An optimal lateral window should suppress migration artifacts at a minimal computational cost. The semblance function in equation 10 appears to have smooth features that simplifies a heuristic choice of the threshold parameters.

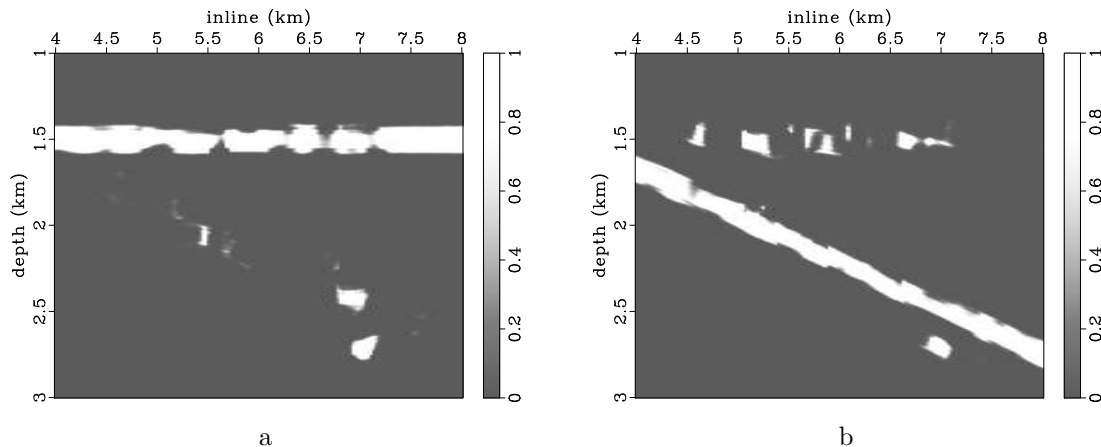


Figure 10: Semblance function for (a) zero-degree partial image and (b) fifteen-degree partial image.

In our synthetic example, we used a dip-angle window of 10 degrees, a lateral window of 150 m, and parameters s_1 and s_2 equal to 0.2 and 0.4, respectively. Figure 11 shows the weighted partial images. Reflectors consistent with the partial images, as well as appropriate parts of the diffraction event, are preserved. At the same time, a large amount of noneffective contribution, which may produce migration noise, has been eliminated. Summation of the weighted partial images provides the stacked image, which has the migration artifacts being suppressed significantly (Figure 12).

A weight function constructed by using the dip-angle direction only allows for attenuating reflection events around their apex areas while preserving diffraction events

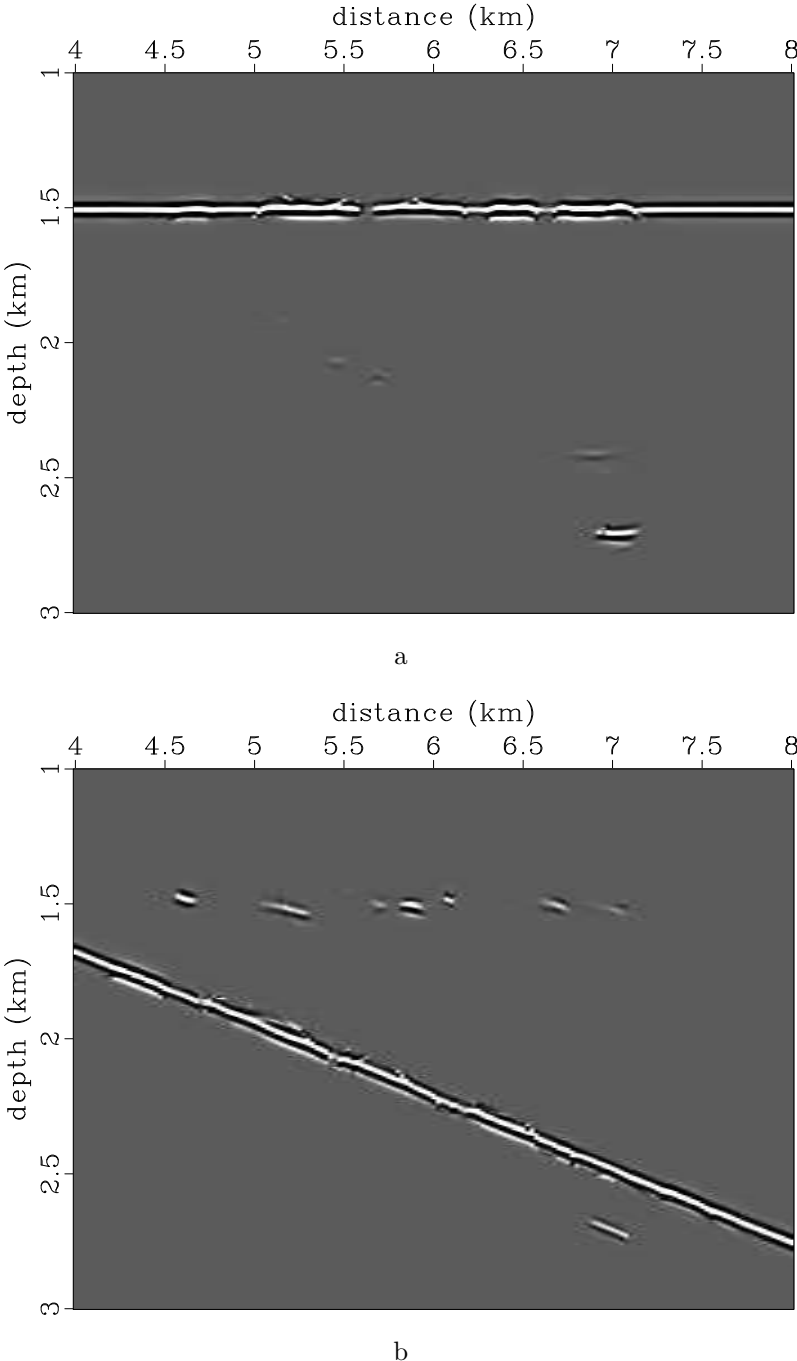


Figure 11: (a) Zero-degree partial image and (b) fifteen-degree partial image after migration-aperture optimization.

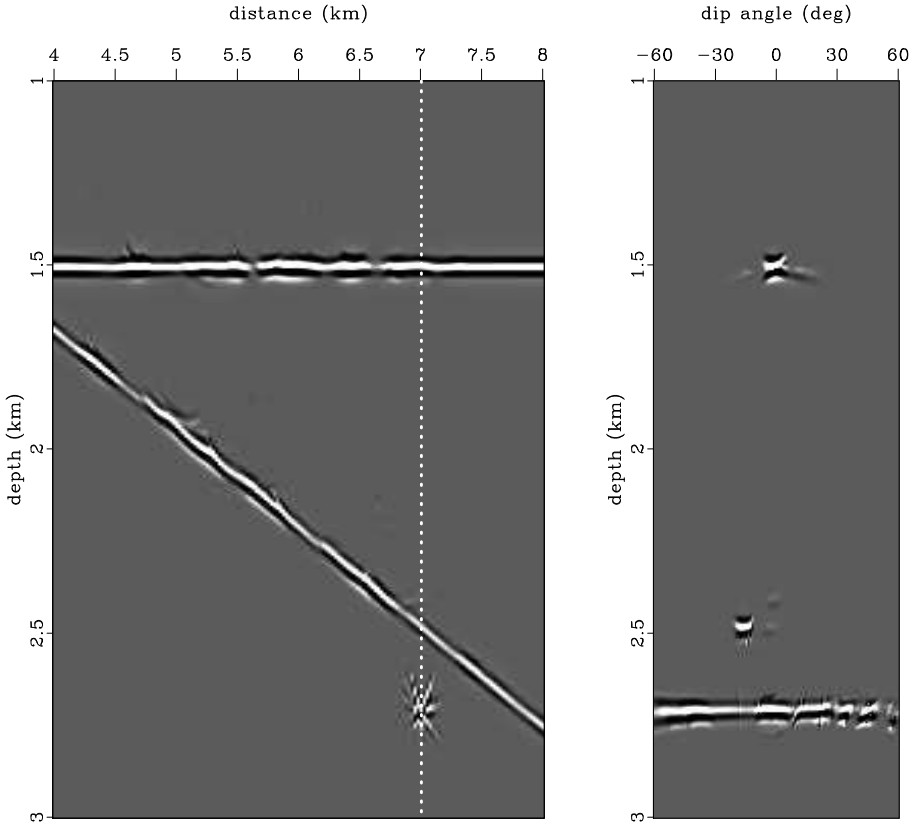


Figure 12: Image and dip-angle gather after migration-aperture optimization by slope-consistency analysis.

as well. Figure 13 shows the result of migrated data weighting using local summation along dip-angle window of 10 degrees. Reflection events are localized around their effective areas, and the diffraction event has its full width being preserved. However, the image remains contaminated by migration artifacts, which happen to be stationary in the dip-angle direction.

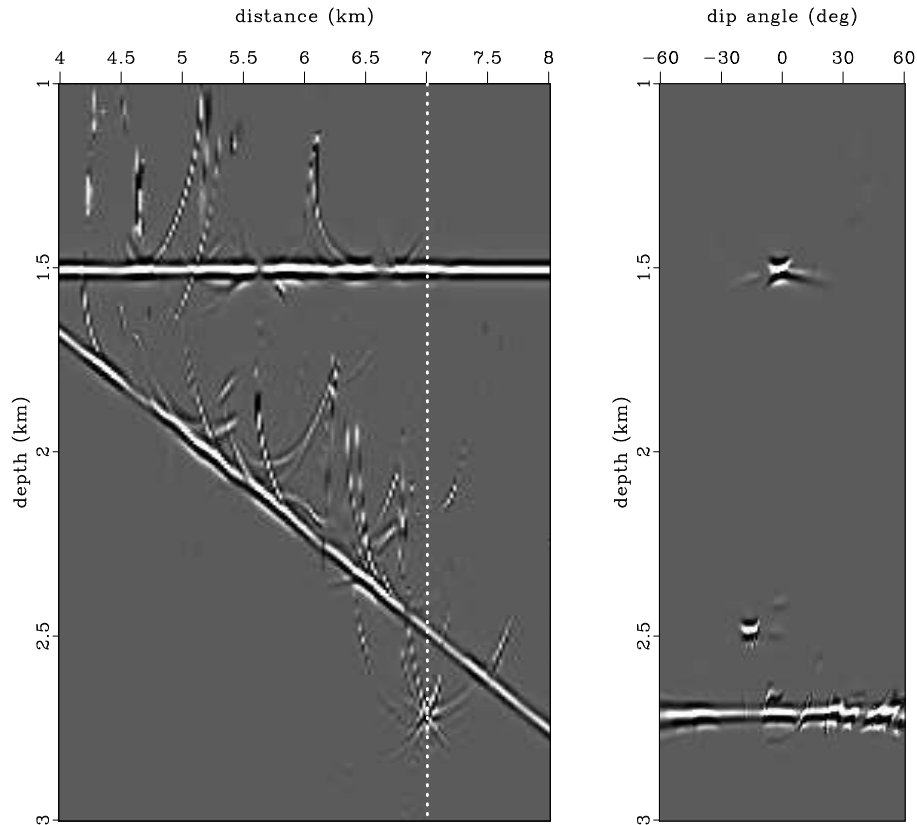


Figure 13: Image and dip-angle gather after migration-aperture optimization by local summation in the dip-angle direction.

We next address the situation when migration velocity is not correct. Figure 14 shows the image and the dip-angle gather after migration with 10% lower velocity. Reflection boundaries look distorted. The diffractor is undermigrated and has a complicated shape in the dip-angle gather. The image is contaminated by strong migration artifacts. For migration-aperture optimization by slope-consistency analysis, we used the same parameters as in the previous example (Figure 15). Reflection and diffraction events both are optimized to their effective parts, eliminating migration noise in the image.

These experiments demonstrate that slope-consistency filtering can be used after migration even when using a complicated velocity model or an incorrect model. In the previous section, we considered theoretically the case of the zero-offset migration. The proposed principles may apply also to prestack migration in which stacking of

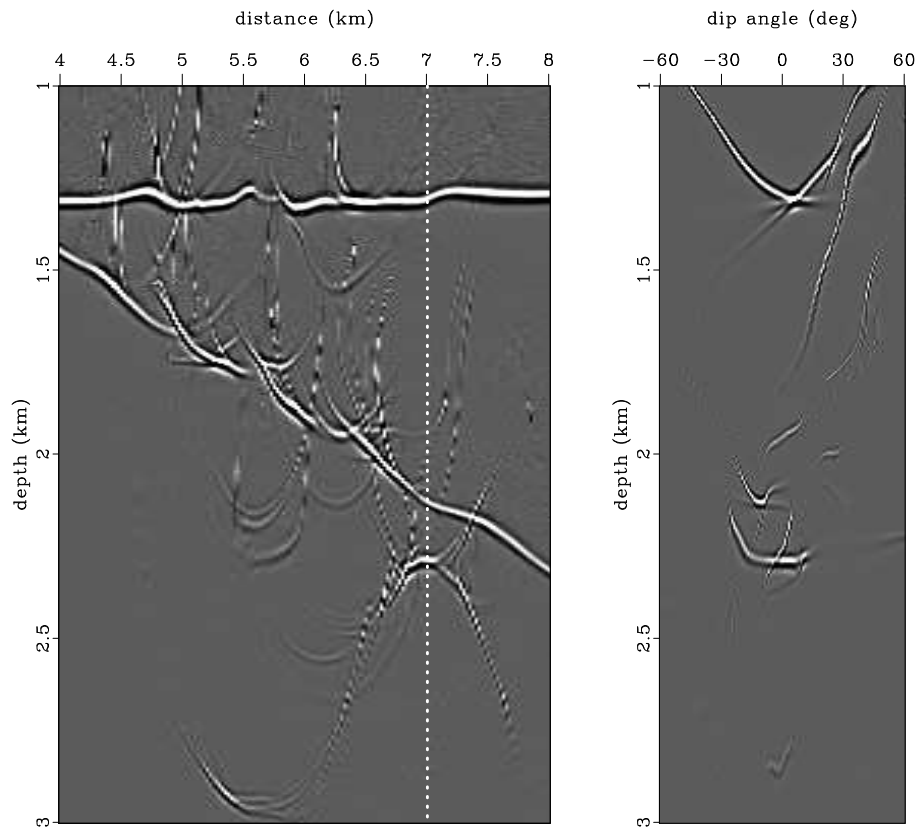


Figure 14: Initial image and common-image-gather in dip-angle domain corresponding to distance of 7 km (wrong velocity case).

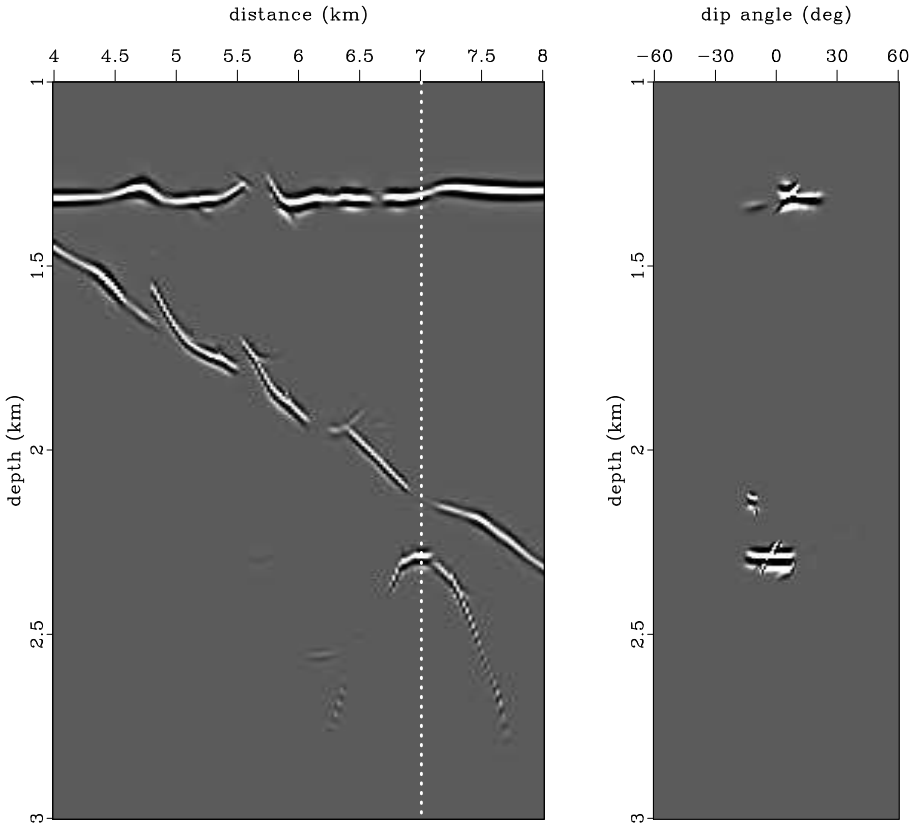


Figure 15: Image and dip-angle gather after migration-aperture optimization by slope-consistency analysis (wrong velocity case).

the full offset range provides accumulation of effective migrated data parts. The experiments also reveal that noneffective segments may have an appropriate slope as well. For instance, the optimized fifteen-degree partial image (Figure 11b) has some events at a depth of 1.5 km. These events appear to have a correct slope that is close to 15 degrees, and they therefore evade nonconsistent-slope filtering and bring noise to the image of the flat reflector. This kind of noise is inherent in Kirchhoff migration and is produced by the complexity of the velocity model and incompleteness of the migrated data (Stolk and Symes, 2004). In practice, it can be eliminated by stacking the full range of offsets.

The proposed approach can be used easily in three dimensions, in which migrated events are defined by two orthogonal directions (Klokov and Fomel, 2012). Migrated constant-dip traces compose a 3D volume, and slope-consistency analysis should be performed along a plane surface whose slope is defined by the two migration dips. The method does not require slope estimation and has a relatively low computational cost.

Note that the effectiveness of the method is conditioned to that of semblance estimation. In the case of conflicting events, semblance operator effectively deals with events that are relatively strong to be detected. In practice, weak diffraction events might get suppressed by reflections and noise, which might cause difficulties in the slope-consistency estimation and, consequently, in the events protection. These weak events can be enhanced by diffraction imaging techniques (Fomel et al., 2007; Klokov and Fomel, 2012).

SYNTHETIC DATA EXAMPLES

We next tested the presented approach on prestack migration of the Sigsbee2B data set (Paffenholz et al., 2002). The model contains a number of artificial point scatterers. The top of the salt body has a high curvature that acts as a transition between reflections and diffractions. There is a number of faults, which produce diffraction energy as well. Therefore, the data set is appropriate for testing of diffraction protection.

Figure 16 shows a seismic image of the left part of the model and one dip-angle gather extracted from the position in which two strong diffraction points are present. The gather contains two flat diffraction events at depths of 5.2 and 7.6 km, which correspond to the artificial scatterers. Some diffraction energy is also found at a depth of 4.3 km scattered by the fault.

Figure 17 shows the image and dip-angle gather after migration-aperture limiting. First, we detected reflection apex positions, estimated effective dip ranges around them, and rejected migrated amplitudes that did not correspond to effective dip intervals. This procedure enables elimination of migration noise with correct imaging of reflection boundaries (Bienati et al., 2009). However, aperture limiting causes significant shortening of diffraction events and, as a result, weakening, or even

disappearance, of diffraction objects in the image.

To optimize the migration aperture using the proposed slope-consistency approach, we performed semblance analysis using a dip-angle aperture of 10 degrees, a lateral base of 200 m, and parameters s_1 and s_2 equal to 0.2 and 0.4, respectively. (Figure 18). Reflection events become limited to the vicinity of their apexes, as in the previous example. At the same time, the procedure protects diffraction events in the gather and, hence, the corresponding diffraction objects in the image. Artificial point scatterers and faults are imaged correctly.

Figure 19a demonstrates one constant-dip partial image corresponding to 15 degrees. It resembles the seismic image of the model, with some differences. As expected, dipping reflection boundaries are shifted from the correct positions and diffraction objects are represented by hyperbolic events. After slope-consistency analysis, we construct a filtering mask (Figure 19b) to protect events whose slope is close to that of the dip of the partial image (Figure 19c). As a result, diffraction hyperbolas became confined to the vicinities of their correct positions, where they have the appropriate slope. Faults at a depth of 4 km and other reflection boundaries were protected as well. Remaining migrated energy was eliminated significantly.

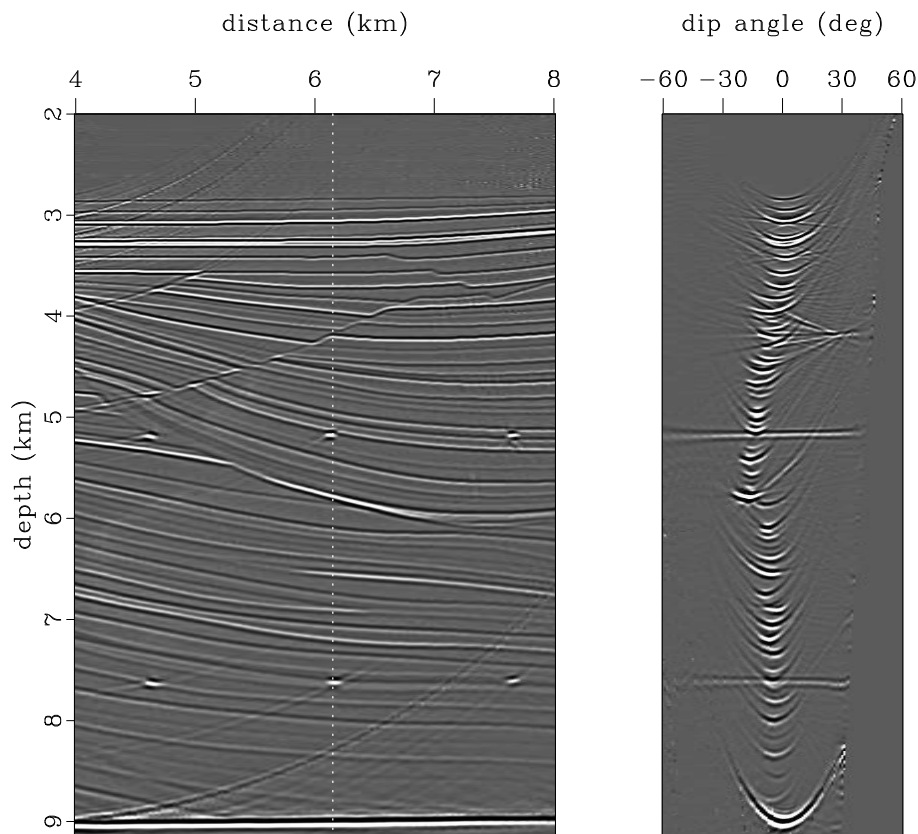


Figure 16: Initial image and common-image gather in dip-angle domain corresponding to distance of 6.1 km.

The salt body complicates Kirchhoff imaging in the right part of the Sigsbee model

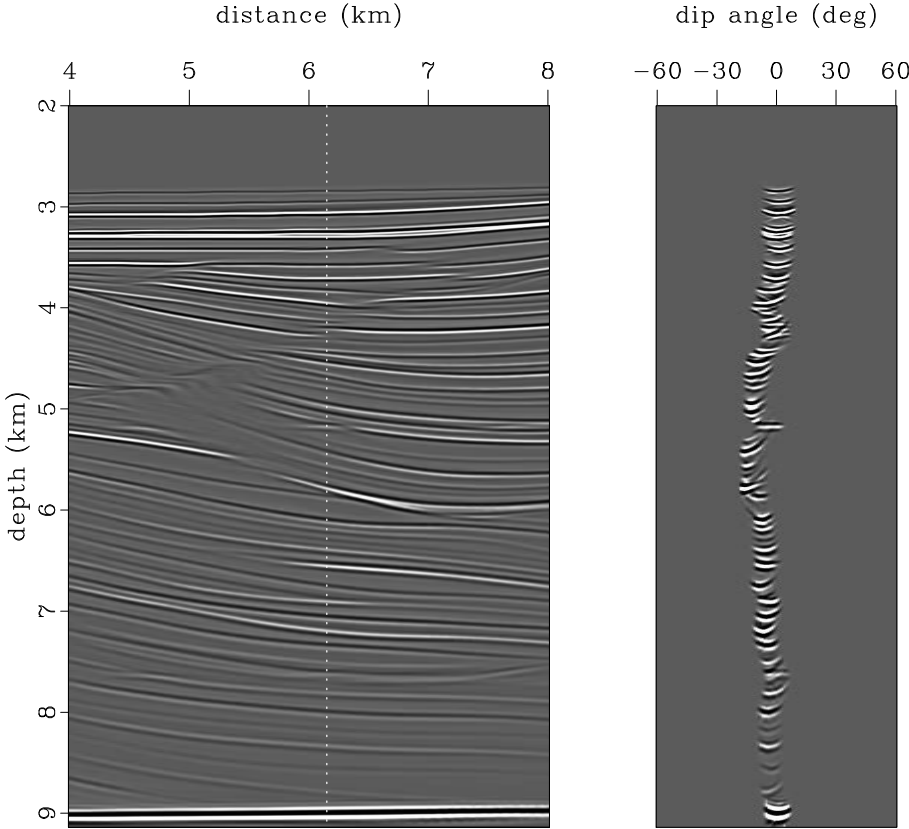


Figure 17: Image and dip-angle gather after migration-aperture limiting.

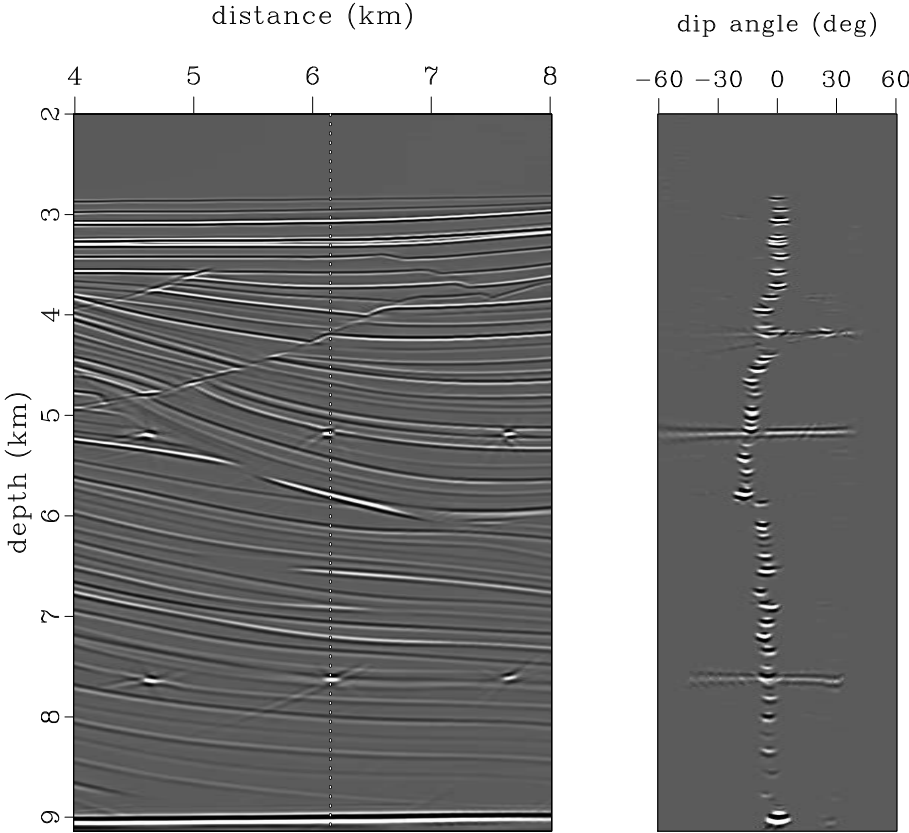


Figure 18: Image and dip-angle gather after migration-aperture optimization by slope-consistency analysis.

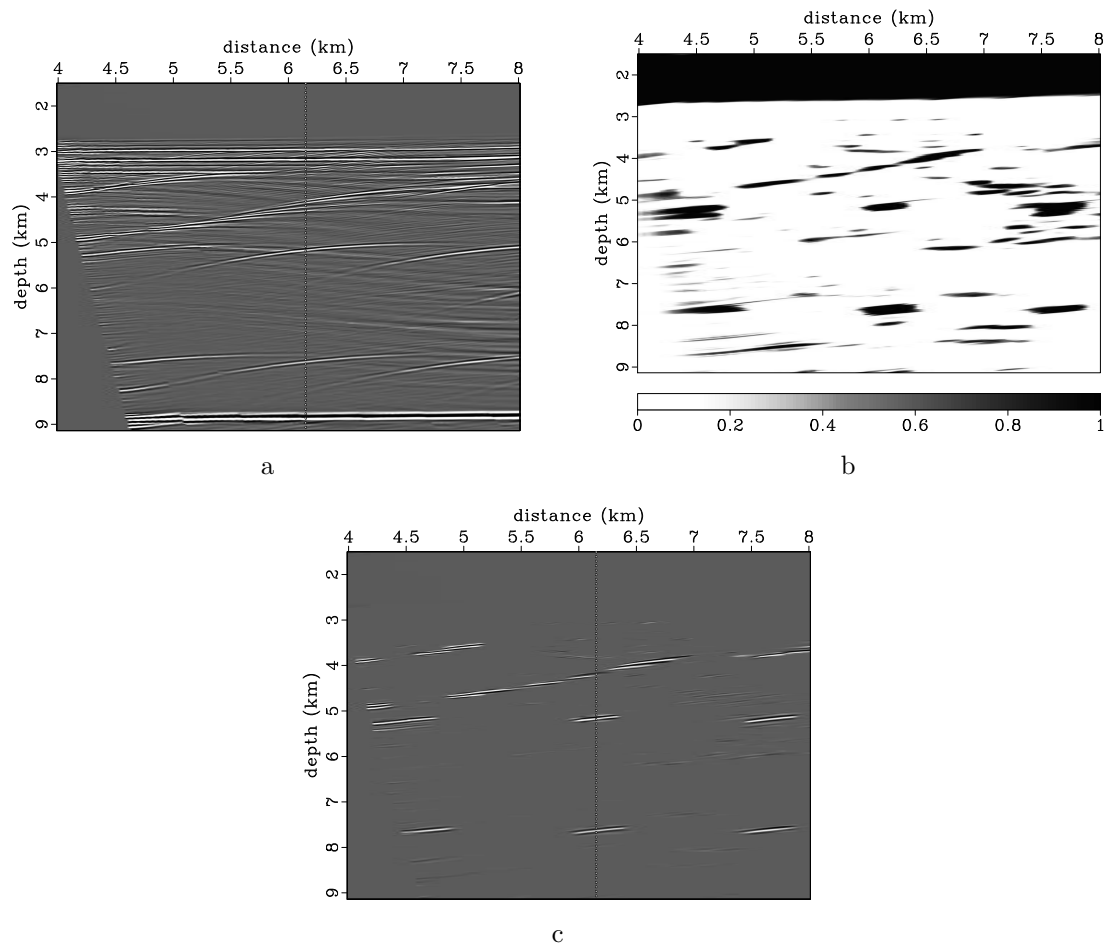


Figure 19: (a) Fifteen-degree constant-dip partial image, (b) weight function produced by slope-consistency analysis, and (c) partial image after migration-aperture optimization. Dashed line indicates position of considered artificial scattering points.

and increases the amount of migration noise. Figure 20 shows a seismic image and one dip-angle gather extracted from the position in which strong diffraction points are present. The scatterer at 7.6 km is illuminated well, and the dip-angle gather contains the corresponding plane diffraction event. A fault can be identified at the 15-km position and depth of 7 km. Some amount of migration noise is concentrated just below the salt and in the salt cavities above.

Migration-aperture optimization by slope-consistency analysis allows us to significantly decrease migration noise and, at the same time, to protect diffraction objects — artificial point scatterers, the fault, and the salt boundary are all imaged correctly (Figure 21). In comparison, simple aperture limiting leads to noise suppression as well; however, the diffraction objects are lost, and the salt body appears distorted (Figure 22).

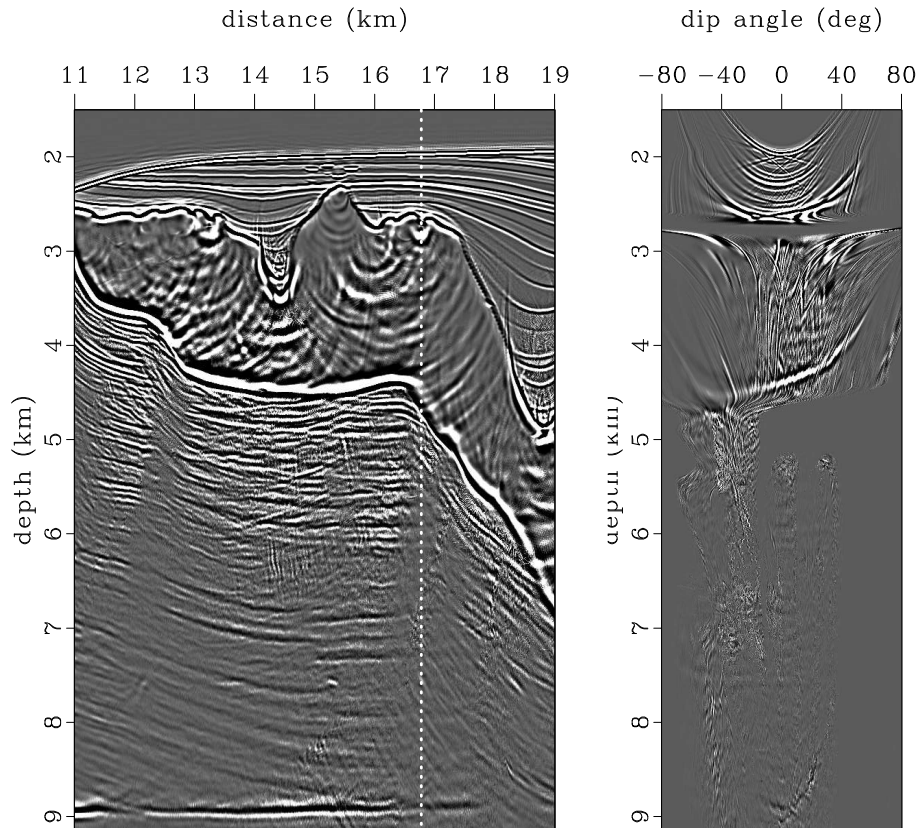


Figure 20: Initial image and common-image gather in dip-angle domain corresponding to distance of 16.8 km.

FIELD DATA APPLICATION

We next applied our aperture-optimization technique to a field 3D data set obtained from the Piceance Basin area in Colorado, USA. Figure 23 shows a part of the Williams Fork Formation, which is a well-known reservoir that contains a number

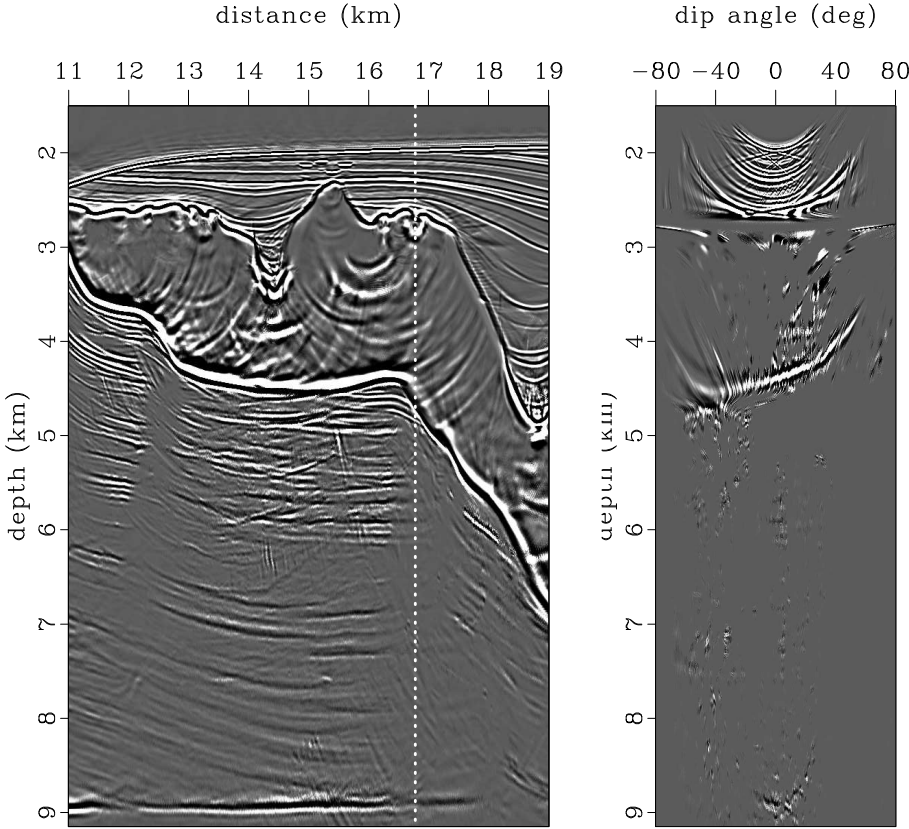


Figure 21: Image and dip-angle gather after migration-aperture optimization by slope-consistency analysis.

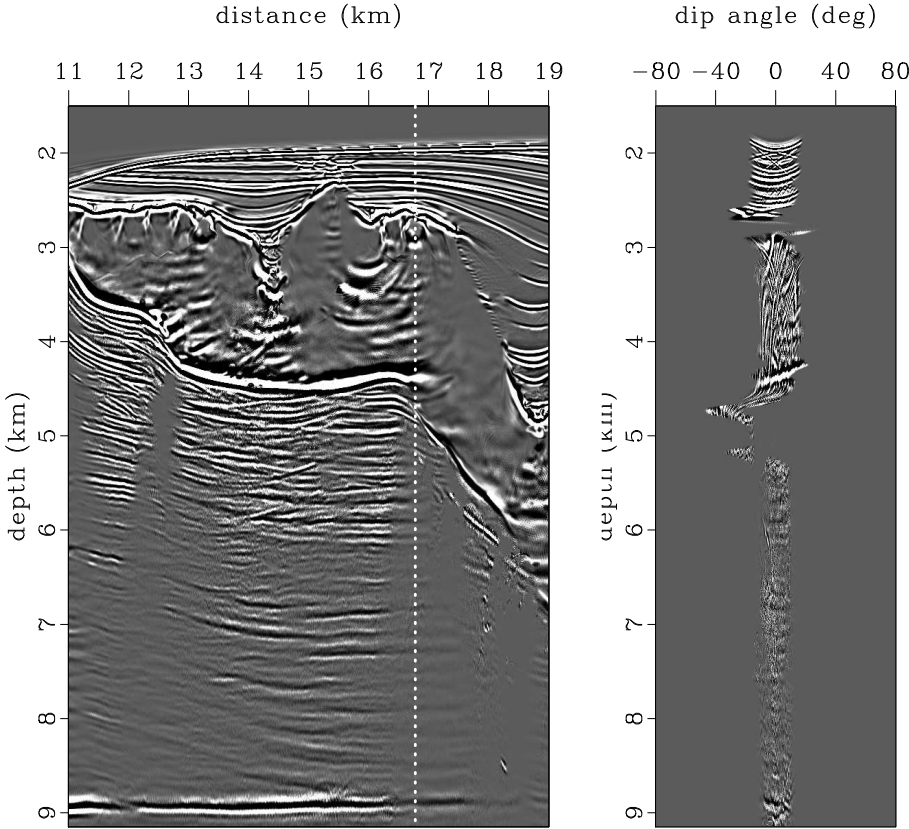


Figure 22: Image and dip-angle gather after migration-aperture limiting.

of channels and point-bar sand bodies (Pranter et al., 2007). Burnett (2011) and Klokov and Fomel (2012) previously analyzed the data by diffraction imaging and showed that a number of diffraction objects were clustered in the top part of the volume. The image is corrupted by migration artifacts, and diffraction objects are buried under the noise.

We performed slope-consistency analysis using a 10-degree dip-angle windows, a 50-m-square stacking base, and parameters s_1 and s_2 equal to 0.1 and 0.3, respectively (Figure 24). Migration noise appears to be filtered out, whereas point objects in the shallow part are preserved. Diffraction objects are clearly observed in the slice.

For comparison, we migrated the data using a limited aperture of 10 degrees in two principal directions (Figure 25). Although most of the migration artifacts have been successfully eliminated, diffraction objects from the top part get smeared. These objects have low energy caused by scarcity of migration dips in the aperture.

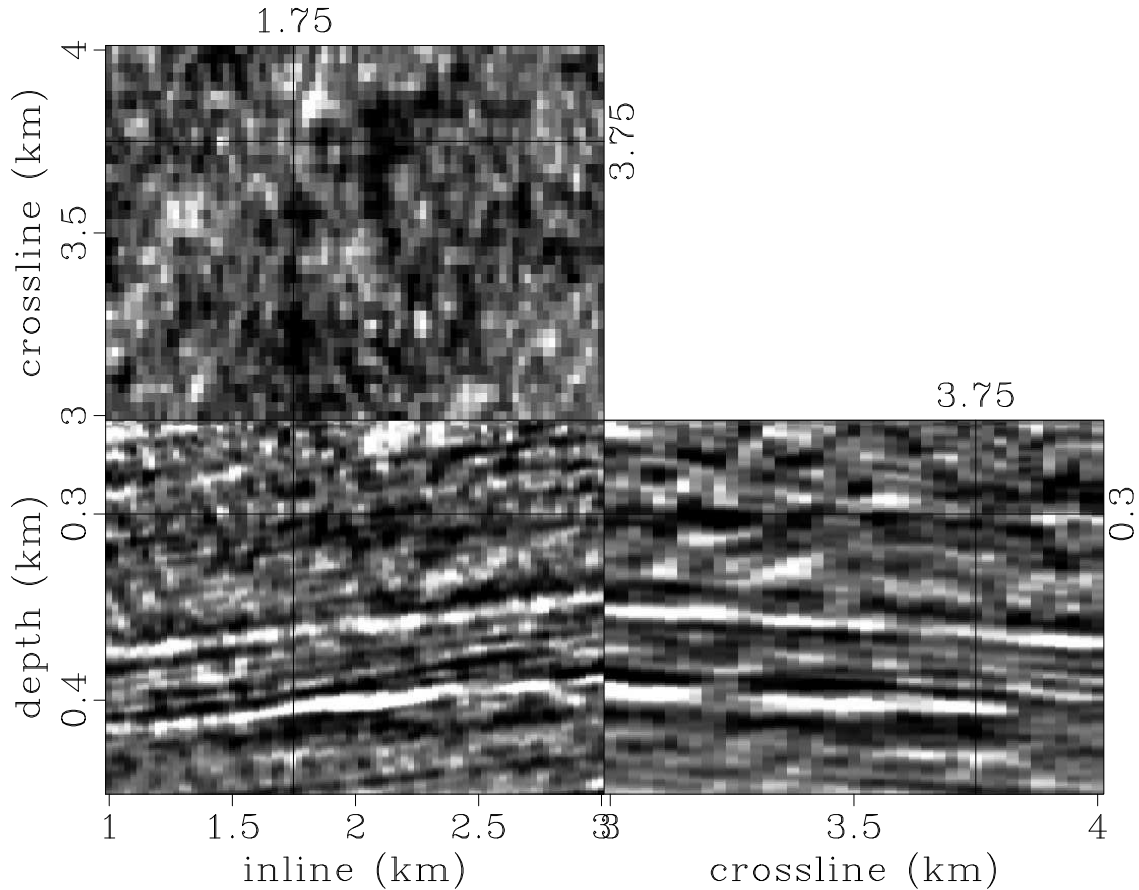


Figure 23: Initial 3D image for Piceance Basin data set.

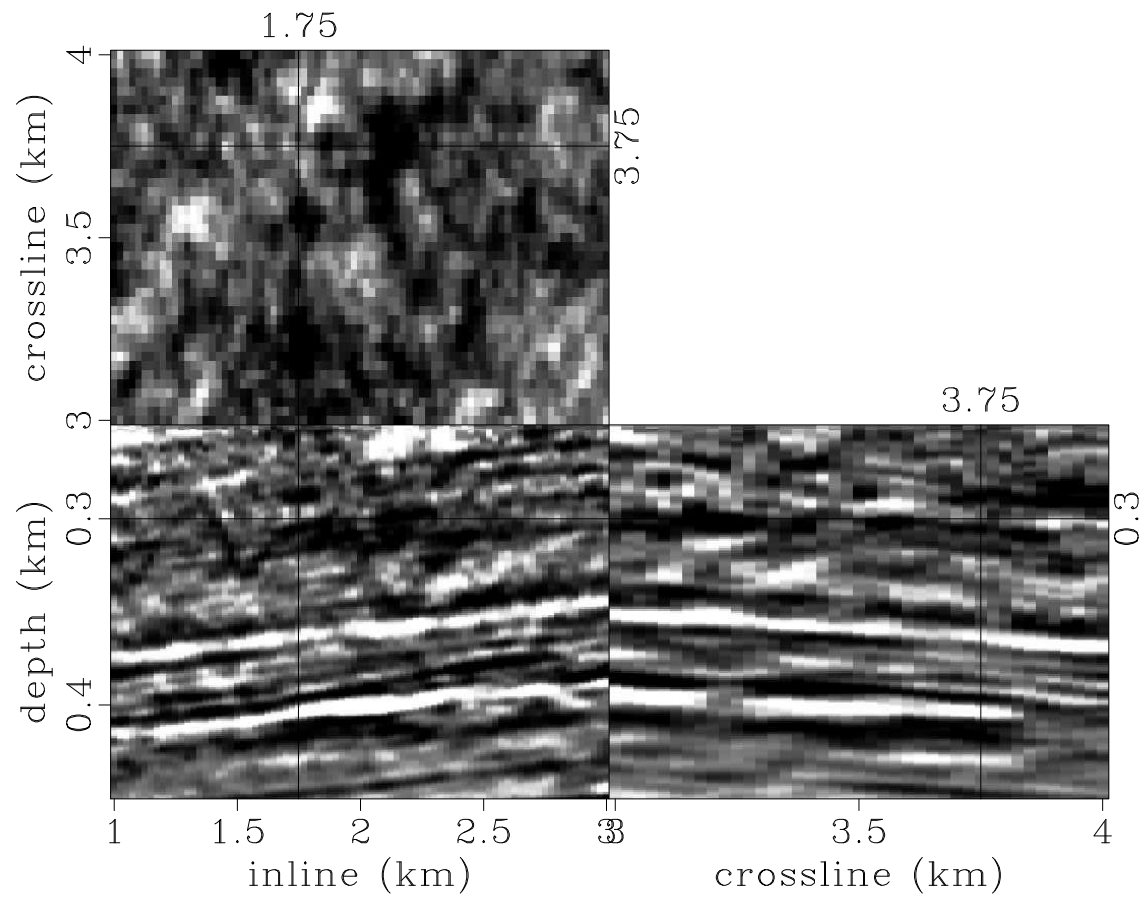


Figure 24: Image after migration-aperture optimization by slope-consistency analysis.

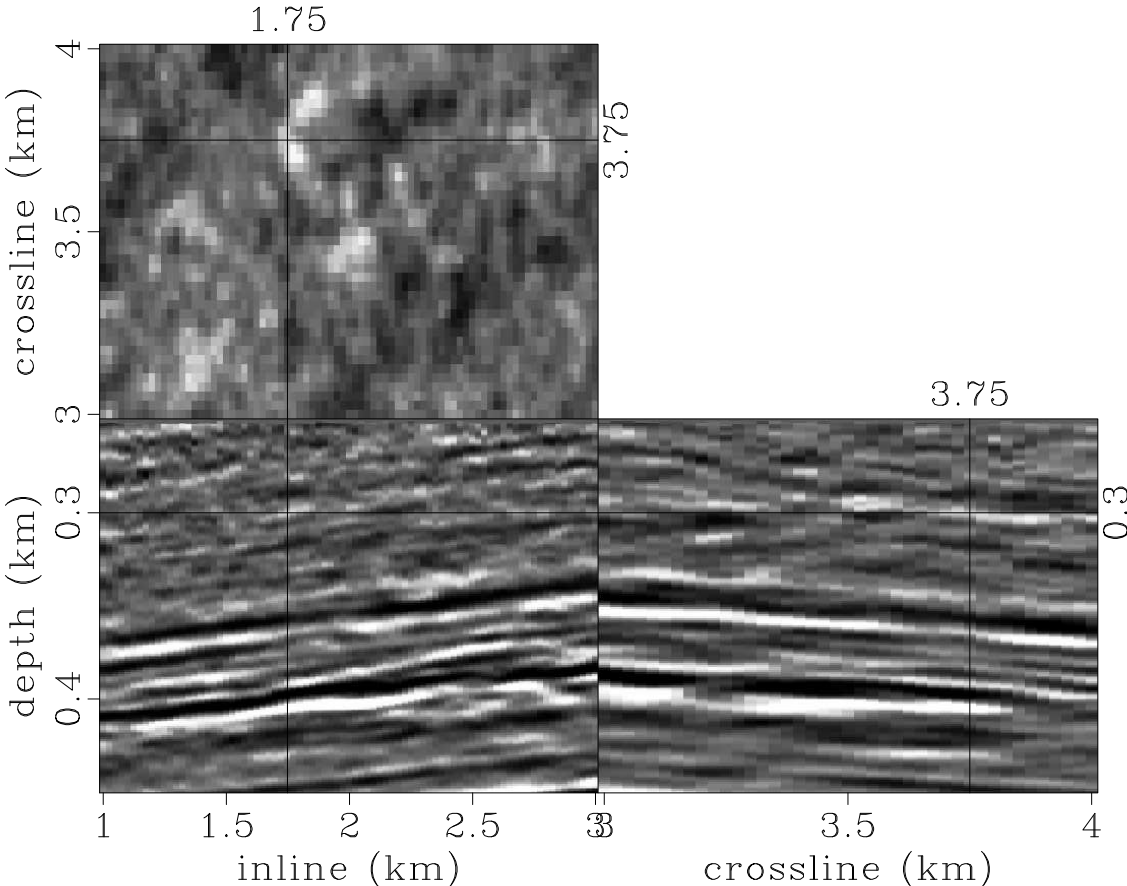


Figure 25: Image obtained after migration with limited aperture.

CONCLUSIONS

Migration-aperture optimization in Kirchhoff angle-domain migration can significantly enhance the quality of a seismic image. The aperture-optimization method needs to eliminate migration artifacts without distorting the useful signal. The diffraction component of the seismic wavefield characterizes small but important geological objects and brings extra resolution to seismic imaging. For an optimal image of diffraction objects, as wide a migration aperture as possible should be used. However, imaging of reflections requires an aperture narrowed around the tangent point.

To meet both requirements, we propose utilizing constant-dip partial images. An analysis of the consistency between local slopes and constant dips of a partial image makes evaluating the contribution of any part of the migrated data possible. This analysis allows us to extract constructive events. Stacking these events is equivalent to migration using an optimal aperture.

ACKNOWLEDGMENTS

We thank Igor Ravve, three anonymous reviewers, and the associate editor Jörg Schleicher for constructive suggestions that improved the paper.

Partial funding for this project was provided by RPSEA through the Ultra-Deepwater and Unconventional Natural Gas and Other Petroleum Resource program authorized by the US Energy Policy Act of 2005. RPSEA (<http://www.rpsea.org/>) is a nonprofit corporation whose mission is to provide a stewardship role in ensuring the focused research, development and deployment of safe and environmentally responsible technology that can effectively deliver hydrocarbons from domestic resources to the citizens of the United States. RPSEA, operating as a consortium of premier US energy research universities, industry, and independent research organizations, manages the program under a contract with the US Department of Energy's National Energy Technology Laboratory.

APPENDIX: HYPERBOLIC REFLECTOR IN THE DIP-ANGLE DOMAIN

For insight into the appearance of reflector images in the dip-angle domain, let us consider the case of a hyperbolic reflector (Fomel and Kazinnik, 2013). A special property of hyperbolic reflectors is that they can transform to plane dipping reflectors or point diffractors with an appropriate choice of parameters. Reflector depth is given by the function

$$z(x) = \sqrt{z_0^2 + (x - x_0)^2 \tan^2 \beta}, \quad (\text{A-1})$$

and zero-offset reflection traveltime is given by

$$t(y) = \frac{2}{v} \sqrt{z_0^2 + (y - x_0)^2 \sin^2 \beta}. \quad (\text{A-2})$$

When the reflector is imaged by time migration in the dip-angle domain (Sava and Fomel, 2003) using velocity v_m , point $\{y, t\}$ in the data domain migrates to $\{x_m, t_m\}$ in the image domain according to

$$x_m = y - \frac{v_m}{2} t \sin \alpha = y - \frac{v_m \sin \alpha}{v} \sqrt{z_0^2 + (y - x_0)^2 \sin^2 \beta}, \quad (\text{A-3})$$

$$t_m = t \cos \alpha = \frac{2 \cos \alpha}{v} \sqrt{z_0^2 + (y - x_0)^2 \sin^2 \beta}, \quad (\text{A-4})$$

where α is the migration dip angle. Eliminating y from equations A-3 and A-4, we arrive at the equation

$$t_m(x_m) = \frac{2 \cos \alpha}{v} \frac{\gamma (x_m - x_0) \sin \alpha \sin^2 \beta + \sqrt{(x_m - x_0)^2 \sin^2 \beta + z_0^2} D}{D}, \quad (\text{A-5})$$

where $\gamma = v_m/v$ and $D = 1 - \gamma^2 \sin^2 \alpha \sin^2 \beta$. Equation A-5 describes the shape of the image of the hyperbolic reflector (A-1) in the dip-angle domain.

When the dip of the migrated event, imaged at a correct velocity ($\gamma = 1$),

$$\tan \alpha_m = \frac{v}{2} t'_m(x_m) = \frac{\cos \alpha \sin^2 \beta}{D} \left[\sin \alpha + \frac{x_m - x_0}{\sqrt{(x_m - x_0)^2 \sin^2 \beta + z_0^2} D} \right], \quad (\text{A-6})$$

is equal to the dip of the image ($\alpha_m = \alpha$), it also becomes equal to the true dip of the reflector ($\alpha_m = \alpha_0$), where

$$\tan \alpha_0 = z'(x_m) = \frac{(x_m - x_0) \tan^2 \beta}{\sqrt{z_0^2 + (x - x_0)^2 \tan^2 \beta}}. \quad (\text{A-7})$$

We can specify these conditions for two special cases described next.

Point diffractor

The hyperbolic reflector in equation A-1 creates a point diffractor at coordinates $\{x_0, z_0\}$ when $\beta = \pi/2$. In this case, equation A-5 simplifies to (Klokov and Fomel, 2012)

$$t_m(x_m) = \frac{2 \cos \alpha}{v} \frac{\gamma (x_m - x_0) \sin \alpha + \sqrt{(x_m - x_0)^2 + z_0^2} (1 - \gamma^2 \sin^2 \alpha)}{1 - \gamma^2 \sin^2 \alpha}. \quad (\text{A-8})$$

At a correct velocity ($\gamma = 1$),

$$t_m(x_m) = \frac{2}{v} \frac{(x_m - x_0) \sin \alpha + \sqrt{(x_m - x_0)^2 + z_0^2} \cos^2 \alpha}{\cos \alpha}, \quad (\text{A-9})$$

which is equivalent to equation 2 in the main text. The dip of the image is

$$\tan \alpha_m = \frac{v}{2} t'_m(x_m) = \tan \alpha + \frac{x_m - x_0}{\cos \alpha \sqrt{(x_m - x_0)^2 + z_0^2} \cos^2 \alpha}. \quad (\text{A-10})$$

It is easy to verify that, above the diffraction point ($x_m = x_0$), $\alpha_m = \alpha$.

Plane dipping reflector

The hyperbolic reflector in equation A-1 becomes a plane dipping reflector when $z_0 = 0$. In this case, equation A-5 simplifies to (Klokov and Fomel, 2012)

$$t_m(x_m) = \frac{2}{v} \frac{(x_m - x_0) \cos \alpha \sin \beta}{1 - \gamma \sin \alpha \sin \beta}. \quad (\text{A-11})$$

The dip of the image at a correct velocity is

$$\tan \alpha_m = \frac{v}{2} t'_m(x_m) = \frac{\cos \alpha \sin \beta}{1 - \sin \alpha \sin \beta}, \quad (\text{A-12})$$

which is equivalent to equation 8 in the main text. The dip of the reflector in this case is simply $\alpha_0 = \beta$. It is easy to verify that when $\alpha = \beta$, $\alpha_m = \alpha$.

REFERENCES

- Alerini, M., and B. Ursin, 2009, Adaptive focusing window for seismic angle migration: *Geophysics*, **74**, S1–S10.
- Audebert, F., P. Froidevaux, H. Rakotoarisoa, and J. Svay-Lucas, 2002, Insights into migration in the angle domain: SEG Technical Program Expanded Abstracts, **21**, 1188–1191.
- Bienati, N., C. Andreoletti, F. Perrone, V. Lipari, and M. Giboli, 2009, Limited aperture migration in the angle domain: 71st EAGE Conference and Exhibition Extended Abstracts, **U005**.
- Bleistein, N., J. Cohen, and W. Stockwell, 2001, *Mathematics of multidimensional seismic imaging, migration, and inversion*: Springer.
- Bleistein, N., and S. Gray, 2002, A proposal for common-opening-angle migration/inversion: Center for Wave Phenomena, **CWP-420**, 293–303.
- Burnett, W., 2011, *Multiazimuth velocity analysis using velocity-independent seismic imaging*: PhD thesis, The University of Texas at Austin.
- Buske, S., S. Gutjahr, and C. Sick, 2009, Fresnel volume migration of single-component seismic data: *Geophysics*, **74**, WCA47–WCA55.
- Dafni, R., and M. Reshef, 2012, Image enhancement by CIG multi-parameter characterization: 74th EAGE Conference and Exhibition.
- Fomel, S., and R. Kazinnik, 2013, Nonhyperbolic common reflection surface: *Geophysical Prospecting*, **61**, 21–27.
- Fomel, S., E. Landa, and M. T. Taner, 2007, Poststack velocity analysis by separation and imaging of seismic diffractions: *Geophysics*, **72**, U89–U94.
- Hertweck, T., C. Jäger, A. Goertz, and J. Schleicher, 2003, Aperture effects in 2.5D kirchhoff migration: a geometrical explanation: *Geophysics*, **68**, 1673–1684.
- Kabbej, A., R. Baina, and B. Duquet, 2007, Aperture optimized two-pass Kirchhoff migration: SEG Technical Program Expanded Abstracts, **26**, 2339–2343.
- Khaidukov, V., E. Landa, and T. J. Moser, 2004, Diffraction imaging by focusing-defocusing: An outlook on seismic superresolution: *Geophysics*, **69**, 1478–1490.

- Klem-Musatov, K., 1994, Theory of seismic diffractions: Society of Exploration Geophysicists.
- Klokov, A., and S. Fomel, 2012, Separation and imaging of seismic diffractions using migrated dip-angle gathers: *Geophysics*, **77**, S131–S143.
- Landa, E., S. Fomel, and M. Reshef, 2008, Separation, imaging, and velocity analysis of seismic diffractions using migrated dip-angle gathers: SEG Technical Program Expanded Abstracts, **27**, 2176–2180.
- Leveille, J. P., I. F. Jones, Z.-Z. Zhou, B. Wang, and F. Liu, 2011, Subsalt imaging for exploration, production, and development: A review: *Geophysics*, **76**, WB3–WB20.
- Lüth, S., S. Buske, R. Giese, and A. Goertz, 2005, Fresnel volume migration of multicomponent data: *Geophysics*, **70**, S121–S129.
- Neidell, N., 1997, Perceptions in seismic imaging part 2: Reflective and diffractive contributions to seismic imaging: *The Leading Edge*, **16**, 1121–1123.
- Paffenholz, J., B. McLain, J. Zaskie, and P. J. Keliher, 2002, Subsalt multiple attenuation and imaging: Observations from the Sigsbee2B synthetic dataset: SEG Technical Program Expanded Abstracts, 2122–2125.
- Pranter, M. J., A. I. Ellison, R. D. Cole, and P. E. Patterson, 2007, Analysis and modeling of intermediate-scale reservoir heterogeneity based on a fluvial point-bar outcrop analog, Williams Fork Formation, Piceance Basin, Colorado: *AAPG Bulletin*, **91**, 1025–1051.
- Sava, P., and S. Fomel, 2001, 3-d traveltimes computation using Huygens wavefront tracing: *Geophysics*, **66**, 883–889.
- Sava, P. C., and S. Fomel, 2003, Angle-domain common-image gathers by wavefield continuation methods: *Geophysics*, **68**, 1065–1074.
- Schleicher, J., P. Hubral, M. Tygel, and M. S. Jaya, 1997, Minimum apertures and Fresnel zones in migration and demigration: *Geophysics*, **62**, 183–194.
- Spinner, M., and J. Mann, 2007, CRS-based minimum-aperture time migration – A 2D land-data case study: SEG Technical Program Expanded Abstracts, **26**, 2354–2358.
- Stolk, C., and W. Symes, 2004, Kinematic artifacts in prestack depth migration: *Geophysics*, **69**, 562–575.
- Sun, H., and G. T. Schuster, 2001, 2-D wavepath migration: *Geophysics*, **66**, 1528–1537.
- Sun, J., 1998, On the limited aperture migration in two dimensions: *Geophysics*, **63**, 984–994.
- Tabti, H., L. J. Gelius, and T. Hellmann, 2004, Fresnel aperture prestack depth migration: *First Break*, **22**, no. 3, 39–46.
- Taner, M. T., and F. Koehler, 1969, Velocity spectra—digital computer derivation applications of velocity functions: *Geophysics*, **34**, 859–881.
- Tillmanns, M., and H. Gebrande, 1999, Focusing in prestack isochrone migration using instantaneous slowness information: *Pure and Applied Geophysics*, **156**, no. 1, 187–206.
- Xu, S., H. Chauris, G. Lambaré, and M. Noble, 2001, Common-angle migration: A strategy for imaging complex media: *Geophysics*, **66**, 1877–1894.